MISTRAL campaign in support of W7-X long pulse operation

Johan W. Oosterbeek[1,*], *Mathias* Stern[1], *Harald* Braune[1], *Karsten* Ewert[1], *Matthias* Hirsch[1], *Frank* Hollmann[1], *Andreas* Killinger[2], *Heinrich.P* Laqua[1], *Philippe* Maquet[3], *Stefan* Marsen[1], *Venancio* Martínez-García[2], *Dmitry* Moseev[1], *Frank* Noke[1], *Sunil* Pak[3], *Arne* Reintrog[1], *Torsten* Stange[1], *Robert C.* Wolf[1], *Rafael J.* Zubieta-Lupo, and *the* W7-X team[1]

[1]Max-Planck-Institut für Plasmaphysik, Teilinstitut Greifswald, Wendelsteinstraße 1, 17491 Greifswald, Germany
[2]University of Stuttgart, Institut für Fertigungstechnologie keramischer Bauteile Allmandring 7b, D-70569 Stuttgart
[3]ITER Organization, Route de Vinon-sur-Verdon, CS 90 046, 13067 St. Paul Lez Durance Cedex, France

Abstract. Following two initial campaigns [1], Stellarator Wendelstein 7-X (W7-X) has now completed the construction phase by installation of active cooling of all plasma facing components. The machine is presently commissioned for the next campaign (OP2) aiming at 1 GJ per pulse, e.g. 100 s at 10 MW, eventually aiming at 18 GJ, e.g. 1800 s at 10 MW. The key heating system is the Electron Cyclotron Resonance Heating (ECRH) system, consisting of 10 gyrotrons with power per gyrotron ranging from 0.6 MW up to 1.0 MW at 140 GHz. A phased upgrade of the installation is in progress with the addition of 2 gyrotrons and the development of 1.5 MW and 2.0 MW gyrotrons, such that at the end of the upgrade 4 gyrotrons will be available in each power class of 1.0, 1.5 and 2.0 MW [2]. The increased ECRH power, combined with O2 and X3 heating schemes at high densities, will lead to increased microwave stray radiation. This is non-absorbed microwave power that diffuses inside the vessel and is incident on all in-vessel components including vacuum windows and attached diagnostic systems. A fraction of the stray radiation is absorbed by resistive or dielectric losses of these components, leading to thermal loads that scale with stray radiation levels and pulse length. At W7-X a high power microwave stray radiation launch facility 'MISTRAL' is available that is used to qualify in-vessel components for use at specified microwave surface power densities [Wm^{-2}]. This paper reports on MISTRAL campaigns in 2020 - 2021 for testing of stray radiation loads during OP2 in W7-X, as well as on an EUROfusion program assessing stray radiation loads on ITER components. A dedicated, absolutely calibrated, caloric load was developed for the campaign to obtain measurement of stray radiation power levels as well as to conveniently expose samples. Amongst other we report on shielding concepts using metal enclosures combined with microwave absorbing coatings and dielectric heating of vacuum windows.

1 Introduction

Electron Resonance Cyclotron Heating (ECRH) or Electron Cyclotron Current Drive (ECCD) are a key actuators in magnetically confined fusion experiments. In optically thick plasmas the absorption of the microwaves is very high but other plasma conditions may apply. A technical issue is a practical limit to the accuracy of the launching angle and polarisation of the microwave beam. Both these physic and technical considerations lead to an inevitable fraction of non-absorbed microwave power that, after many passes through the vessel and the plasma, diffuses into microwave stray radiation. This power is incident on the vessel interior resulting in thermal loads but also propagates through ports interfering with diagnostic operation. These problems are actively worked on in the community and in this paper we report on recent work using the MISTRAL stray radiation exposure facility: reduction of stray radiation, response of microwave absorbing coatings and stray radiation exposure of vacuum windows.

2 MISTRAL

The Microwave Stray Radiation Exposure Facility 'MISTRAL' is a large resonator in which a microwave stray radiation field is generated to qualify components for stray radiation loads in the vessel [3–6]. It is a tube with length 2 m and a diameter of 1.5 m. A gyrotron Gaussian beam at 140 GHz is injected through a sapphire vacuum window into the vessel where reflects off a mirror with two inclinations: a large inclination directing the beam to the vessel circumference such that the beam makes a trajectory around the inner circumference (Fig. 1a), and a small inclination directing the beam towards the long side of the tube such that it also propagates along the vessel (Fig. 1b.) On each bounce off the vessel wall some of the beam power is scattered towards the centre of the vessel resulting in a microwave stray radiation field in the centre region of the vessel. The reflecting mirror is in fact V-shaped such that two beams are generated, one travelling clockwise, as shown in Fig. 1a), and one travelling counter clockwise. By adjustment of gyrotron settings and duty cycle the CW input power can be set up to 10 kW. The high wall reflectivity combined with modest size apertures leads to a surface

---

power density of p = (55 ± 5) kWm^{-2}. This was measured with a caloric load which was developed for the work described here and is located near the centre of the vessel closure plate when viewing the face in Fig. 1a). A cartoon of the caloric load arrangement is shown in Fig. 2. Samples such as vacuum windows or filters may be mounted in the sample holder. In the interior Teflon hoses with a steady water flow are mounted. The low refractive index of Teflon combined with the high absorption of the water and the reflecting cone at the far end ensure a very low reflection coefficient, of the order of 2%. In the cone a pyrometer is mounted to monitor the temperature of samples in the sample holder. More details are available in [7].
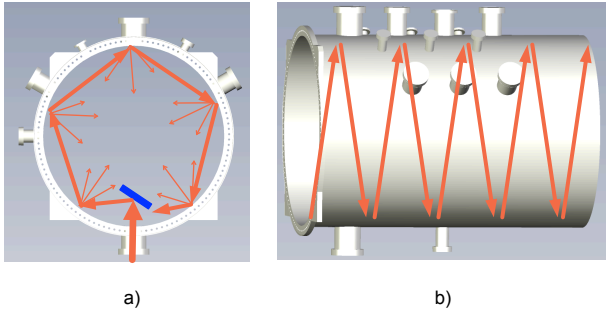

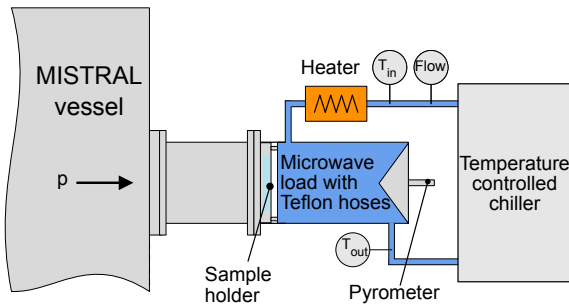**Figure 1.** Conversion of collimated beam to stray radiation.

Figure 2. Caloric load attached to MISTRAL DN150 port.

3 Reduction of stray radiation

Full metallic shielding of components against stray radiation is not always possible. Effort is then directed towards using low-loss components, providing sufficient thermal sink and measures to reduce stray radiation levels. In this section, the reduction of stray radiation in a sub-volume by limiting the input stray radiation level combined with the use absorbing coatings is discussed. A detailed model for analysing coupled cavities is found in [8, 9].

3.1 Surface power densities in coupled cavities

Often the task is to reduce stray radiation levels inside a sub-volume in the vessel or in a system attached to the vessel. The most basic model is that as depicted in Fig. 3. The large volume is considered to be a constant source of
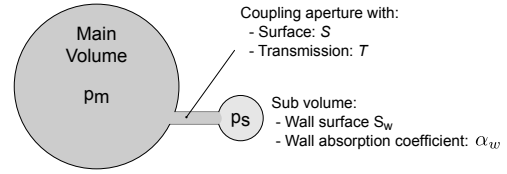

Figure 3. Cartoon of coupling between a main volume with surface power density p_m and a small sub-volume with surface power density p_s.

stray radiation with surface power density p_m. The sub-volume is shown attached to the vessel, such as a diagnostic, but it could also be a structure inside the vessel such as an ECW launcher or a divertor enclosure. An intuitive measure is to reduce the surface power density in the sub-volume by reducing the coupling: making the aperture surface S smaller or by placing a filter in the aperture with a low transmission coefficient T for microwaves. But this may not necessarily lead to a reduction of the surface power density inside the sub-volume as in equilibrium the surface power density is determined by the power that flows into the sub-volume AND the losses inside the sub-volume. This is best seen using the power balance:

$$p_m \cdot S \cdot T = p_s \cdot S \cdot T + p_s \cdot S_w \cdot \alpha_w \Leftrightarrow \quad \text{(1a)}$$

$$\frac{p_s}{p_m} = \frac{S \cdot T}{S \cdot T + S_w \alpha_w}, \quad \text{(1b)}$$

with the symbols are defined in the sketch in Fig. 3. It is seen that in the limit of loss-less walls the surface power density in both cavities is the same. But placing absorbing material in the sub-cavity allows to significantly lower the surface power density in the sub-cavity. This is illustrated in Fig. 4. This does not go at the cost of massive dissipation as the product ST can be lowered by e.g. a reduced aperture or a filter. A practical application of this is the stray radiation protection of the pressure gauges on the MISTRAL. The gauges are mounted on the pumping lines to the turbo pumps. A wire mesh was placed over the pumping aperture and a microwave absorbing coating was placed inside the port, see the photo in Fig. 5. For the selection of the mesh 3 commercially available meshes of different wire and mesh size (unit: lines per inch) were purchased and tested in the sample holder. Four measurements were taken: 1) no mesh, and 2-4) with meshes. The mesh transmission is found by normalising the calorimeter power with mesh to the measurement with no mesh. The results are shown in Fig. 6. For use in the MISTRAL the 24 lines/inch mesh was selected as it resulted in low enough stray radiation levels, being mechanically strong and not impeding the pumping speed too much.

3.2 Absorbing coating

Stray radiation levels can be lowered by dissipation of the microwaves. The losses can be introduced by application of a microwave absorbing coating on metal surfaces [10–12]. This is practical as a thin layer can applied with Atmospheric Plasma Spraying onto walls or pipes, providing
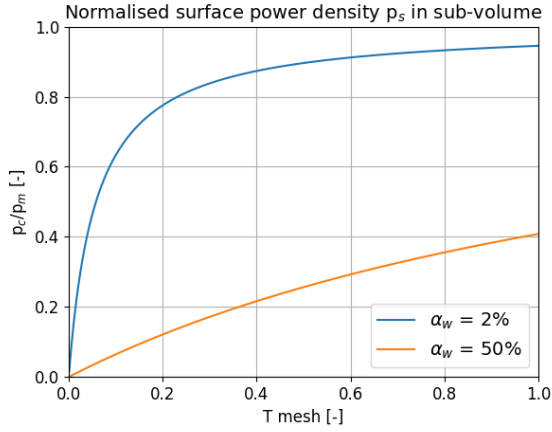
Figure 4. Reduction of stray radiation by using a wire mesh filter with transmission T and for two different wall absorption coefficients. While a coating with up to 75% absorption was demonstrated, 50% is shown in the example as usually not all walls are, or can be, coated.
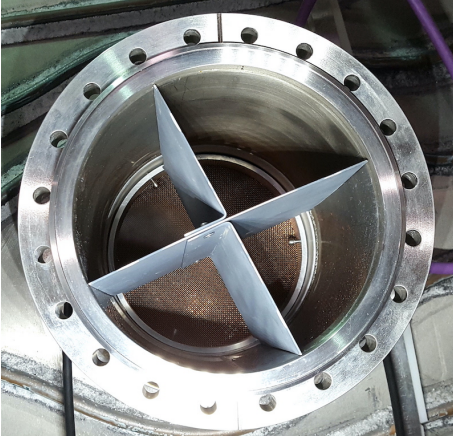

Figure 5. Protection of the vacuum gauges in the pumping port. The photo is take outside the MISTRAL with the vacuum pumps removed. At the far end of the port (vacuum side) the mesh is seen. The insert is a microwave absorber: an aluminum sheet coated with a microwave absorbing layer, refer to section 3.2.

a heat sink at the same time. Another advantage of a coating in the mm-wave region is that the thickness can be set such that the electric field reflection coefficient on the surface is minimised, leading to a maximum in absorption. This is caused by multiple internal reflections inside the layer. The resonance occurs under the condition $d = m\frac{1}{4}\lambda$, with d the coating thickness, m an odd integer (1, 3, $\cdots$) and λ the wavelength inside the dielectric, which is the vacuum wavelength λ_0 divided by the square root of the relative permittivity. The reflection can also be maximised, leading to a minimum in the absorbed fraction. The anti-resonant condition is $d = n\frac{1}{2}\lambda$, with n an integer (1, 2, $\cdots$). Absorption is quantified using plane wave propagation: $E = E_0 e^{j\omega t - \gamma z}$ where $\gamma = \alpha + j\beta$ is the propagation constant with α the attenuation constant and β the phase constant $2\pi/\lambda$. As the electrical field propagates into the
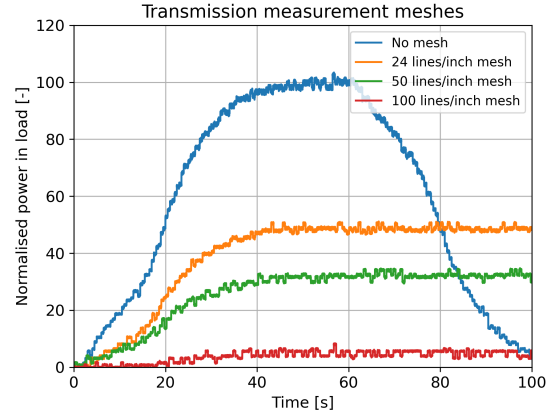
coating it exponentially decays: $E(z) = E_0 e^{-\alpha z}$, while the power decays as $P(z) = P_0 e^{-2\alpha z}$. The attenuation constant is determined by the losses in the coating. These are found by the current densities in the coating [13]:

$$J = j\omega\epsilon' \left(1 - j\left[\frac{\sigma_a}{\omega\epsilon'} + \frac{\sigma_s}{\omega\epsilon'}\right]\right) E \qquad (2)$$

The three terms left to right are: i) the loss-less displacement current density, ii) a loss current density induced by the alternating field (σ_a), and iii) a loss current density caused by a finite static conductivity (σ_s). In the expression ϵ' is the real part of the complex permittivity, which is defined as $\epsilon = \epsilon' - j\epsilon'' = \epsilon_0 (\epsilon_r' - j\epsilon_r'')$. The imaginary part ϵ'' is defined by the relation $\sigma_a = \omega\epsilon''$. It is common to express the dielectric losses by the loss tangent $\tan\delta_a = \epsilon''/\epsilon'$. One then obtains for the ratios between the square brackets: $\tan\delta_a + \sigma_s/\omega\epsilon'$. These are physically different: the measure for dielectric losses and the measure for ohmic losses, however, with the MISTRAL at a single frequency, they cannot be distinguished [14] and they lead to a net heating rate ($\Delta T/\Delta t$) of the coating. In experiment and modelling at the MISTRAL therefore the two terms are replaced by a single measure for conduction losses: $\tan\delta$, noting that this is not necessarily the dielectric loss tangent as quoted for ceramics.

The coating response is evaluated by illumination with a plane wave. The propagation constant γ of the wave is obtained by using both Maxwell equations and substituting a plane wave solution. This results in:

$$\gamma = j\omega \sqrt{\mu_0 \epsilon_0 \epsilon_r'} \sqrt{1 - j\tan\delta} \qquad (3)$$

Following the methodology for a vacuum window as in [7], plane wave propagation inside the coating is modelled by considering the layer to be a lossy ceramic but now terminated with a reflecting metal wall. See the schematic in Appendix A. For instruction only normal incidence is shown but the full model includes oblique incidence. An additional change, following Hentrich [12], is the using

the complex permittivity in computation of the refracted angle in the layer as opposed to taking only the real part. This has been applied too for computation of the layer impedance. This is required as, contrary to low-loss vacuum windows, the imaginary part of the complex permittivity may no longer be much smaller as the real part.

The coating used in this work is an Al_2O_3/TiO_2 coating [10–12], mixed to ratio 87% / 13%. For this coating Hentrich [14] extracted a 0.25λ resonance thickness of 165 μm at 140 GHz. MISTRAL measurements (section 4.3) showed an absorption coefficient of 75% at a thickness of 150 μm. Using the data a fit was made using a complex permittivity with $\epsilon'_r = 11.2$ and $\tan\delta = 0.16$, see Fig. 7. In the experiment a coating with 300 μm thickness showed 33% absorption. This is in broad agreement with the model. Evaluation of the substrate surface resistance R_s shows this to be an insensitive parameter in the model: as long as a metal is used, the response is the same within fractions of a percentage point.
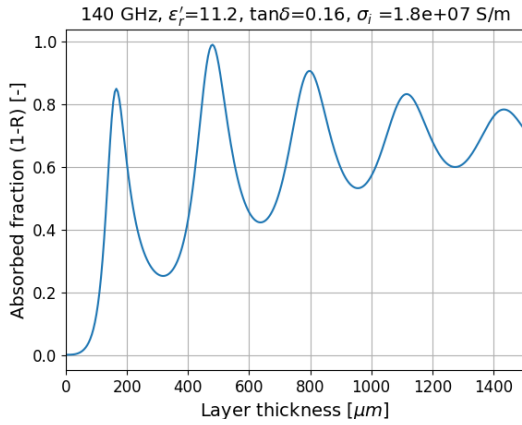

Figure 7. Modelled absorbed fraction (1-R) in coating fitted to experiment data. The maxima and minima are caused by multiple internal reflections. At larger thickness these fade and the absorption converges to $1-R_i$, with R_i the initial reflected fraction off the boundary. The model shows even larger absorption at next two maxima. These are not experimentally verified but result from larger bulk absorption (longer optical path) coinciding with maxima due to multiple internal reflections.

The model was next used to investigate the response at oblique incidence. This shows, besides the effect of the Fresnell equations, little variation with incidence angle. This is explained, as also noted by Hentrich [12], by only small differences in optical path due to the small refracted angels given the high relative permittivity.

The stray radiation response is now found following the methodology in [7]. In short: the coating is exposed to isotropic stray radiation which is modelled by an angular spectrum of incidence angles with a normal distribution and considering both polarisations. The normal distribution is important as large incidence angles are more pronounced as small incidence angles, which may be understood by considering the rays to be incident through a virtual dome placed over the coating. The modelled isotropic stray radiation response of the coating is shown

in Fig. 8. In the plot the x-axis shows the maximum considered incidence angle θ_i, for example: $\theta_i = 20°$ means an isotropic stray radiation response when considering angles up to 20°. The plot shows the absorbed fraction for the res-
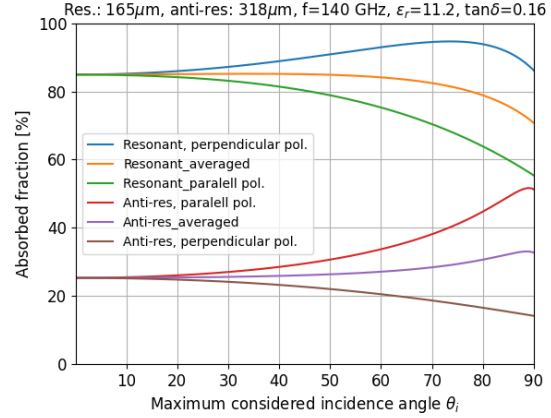

Figure 8. Modelled isotropic stray radiation response with input data from Fig. 7. Upper traces: resonant, 165 μm, lower traces: anti-resonant, 318 μm. The absorbed fractions are plotted as a function of considered range of incident angles, e.g. $\theta_i = 0°$ is normal incidence while $\theta_i = 20°$ includes all incidence angles up to 20°. For each thickness the response to perpendicular and parallel polarisation is plotted. The averages of these (label 'averaged') is the overall isotropic stray radiation response.

onant layer and the anti-resonant layer. For each layer the stray radiation response for either polarisation is shown (perpendicular and parallel). For a layer, the average of both polarisations predicts the isotropic stray radiation response. The data for minima and maxima at normal incidence has been taken from Fig. 7. The predicted isotropic stray radiation response as function of considered rage of incidence angles shows a flat response, except for a modest effect when including the very large incidence angles.

These modelling results together with absorbed fractions of stray radiation power measured (section 4.3) are consistent with a scan over fixed angles by Hentrich [12]. This allows to conclude that the absorbed fraction of power using stray radiation exposure is not significantly affected by the angular distribution of the stray radiation.

Measurement and modelling was all at 140 GHz in this work. It is worth noting that in case the dielectric heating is dominant, the coating absorption at frequencies not too far off, say at 170 GHz, will be the same as long as the layer thickness is adapted to this new frequency too. This may be seen as follows. In case the loss tangent is no too excessive one can approximate α by $\pi\sqrt{\epsilon'_r}\tan\delta f/c$ [7]. The attenuation goes as $e^{-2\alpha d}$, but as $d = 0.25(1/\sqrt{\epsilon'_r})(c/f)$, the scaling with frequency and layer thickness cancels out.

4 Vacuum Windows

The work on vacuum window exposure during the MISTRAL campaigns in 2020 and 2021 addressed three topics: i) stray radiation loads in vacuum windows, ii) expo-

sure of ITO-coatings on vacuum windows, and iii) prototype test of ITER window stray radiation sensors.

4.1 Stray radiation loads in vacuum windows

The isotropic stray radiation response of vacuum windows is reported in [7]. The work is summarised here.

Vacuum windows are critical components, yet considerable thermal loads may result due to dielectric heating by microwave stray radiation. For low-loss windows the absorbed fraction of power can be computed accurately using the loss tangent and the permittivity. But two questions are frequently raised: i) what is the loss tangent at microwave frequencies? and ii) what is the isotropic stray radiation response? To address these questions the permittivity and loss tangent at 140 GHz for a number of commercially available windows were measured using a collimated beam at low power in the laboratory [15, 16]. The stray radiation response was next measured and modelled at high power in the MISTRAL.

The outcome of the work is that, for a window in a typical port geometry, i.e. by excluding the very large incidence angles, the single pass absorbed fraction may be taken as a upper limit by isotropic stray radiation, while applying a safety margin $(1 + \epsilon_r')/2\sqrt{\epsilon_r'}$. As the single pass absorption is easily calculated using the permittivity and loss tangent, laboratory data is now sufficient to get the high power load.

4.2 ITO-coated windows

In order to reduce the stray radiation transmitted through a vacuum window an ITO-coating may be applied. This is an Indium Tin Oxide layer which has a surface resistance inversely proportional to the ITO-conductivity and the layer thickness. Note that the surface resistance has unit $\Omega/\square$ as it is defined with the wave incident on a symmetrical surface [17]. Using data extracted from coatings in use at W7-X, the surface resistance is plotted as function of layer thickness using $R_c = 1/(\sigma_c \tau)$ [17], with σ_c the thin layer ITO conductivity and τ the layer thickness, see Fig. 9. Then, using transmission line theory, the reflected fraction of power due to an impedance step from air $\rightarrow$ ITO is computed, see Fig. 10. Exposure of ITO-coated windows in the MISTRAL confirm that relatively thick coatings, having a surface resistance 20 $\Omega/\square$ or less, show very high stray radiation reflection, comparable to reflection off a metal surface. As a consequence, there is very little absorption inside the ITO coating. On the other hand, very thin coatings with high surface resistance show high transmission and high ITO-induced absorption, resulting in poor attenuation of stray radiation and excessive window heating rates. A practical issue is that an ITO-coating close to the plasma may be eroded by it. The coating must then be on the air-side of the window. While this still gives the large reduction in transmission for stray radiation, it results in double pass absorption in the window which may now cause a considerable thermal load.
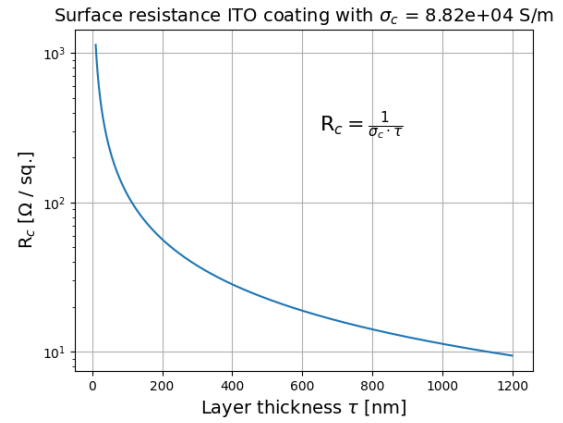

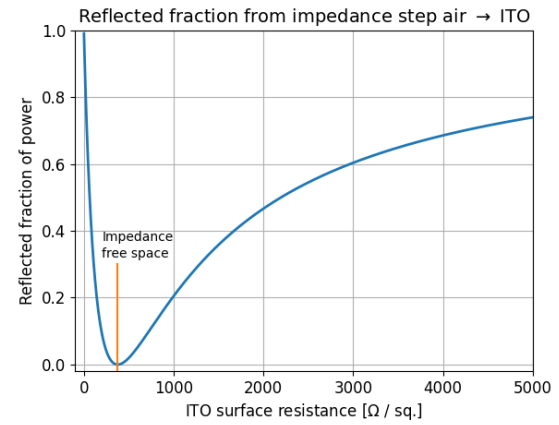**Figure 9.** ITO surface resistance as function of layer thickness.

Figure 10. Reflection due to impedance step air $\rightarrow$ ITO-layer.

4.3 ITER stray radiation sensors

A novel development at ITER [18] are stray radiation window sensors. These are Molybdenum rings with a microwave absorbing coating that are placed at the edge of the window aperture. A prototype test was made at the MISTRAL, the arrangement is shown in Fig.11. At three locations of the ring the temperature is measured with an embedded thermocouple. The absorbing coating is as described in section 3.2. Figure 12 shows the heating rate for a ring with an almost resonant layer thickness (150 μm), for a ring with an almost anti-resonant layer thickness (270 μm) and for a ring with an anti-resonant layer (300 μm). The stray radiation exposure was p = (53 ± 5) kWm^{-2}. The heating rate is equated to the specific density giving the power flowing into the body. This is the absorbed power by the coating: $P_{abs} = p \cdot A \cdot S_e$, with S_e the exposed surface of the coated ring. Equating the two gives the absorbed fractions: $A_{150} = 75\%$ and $A_{270} \approx A_{300} = 33\%$, both with relative error of 10%. Having found the absorbed fractions in situ, the sensors are calibrated and can be used to provide the incident surface power density from the measured heating rate. At modest temperature linear scaling
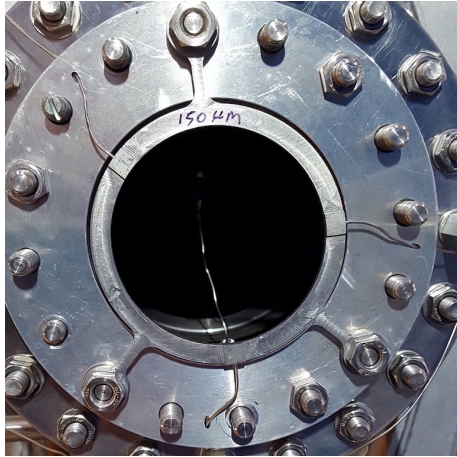
Figure 11. ITER window sensor mounted on MISTRAL port.

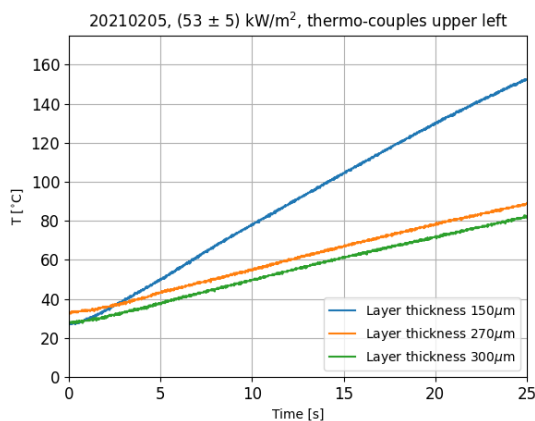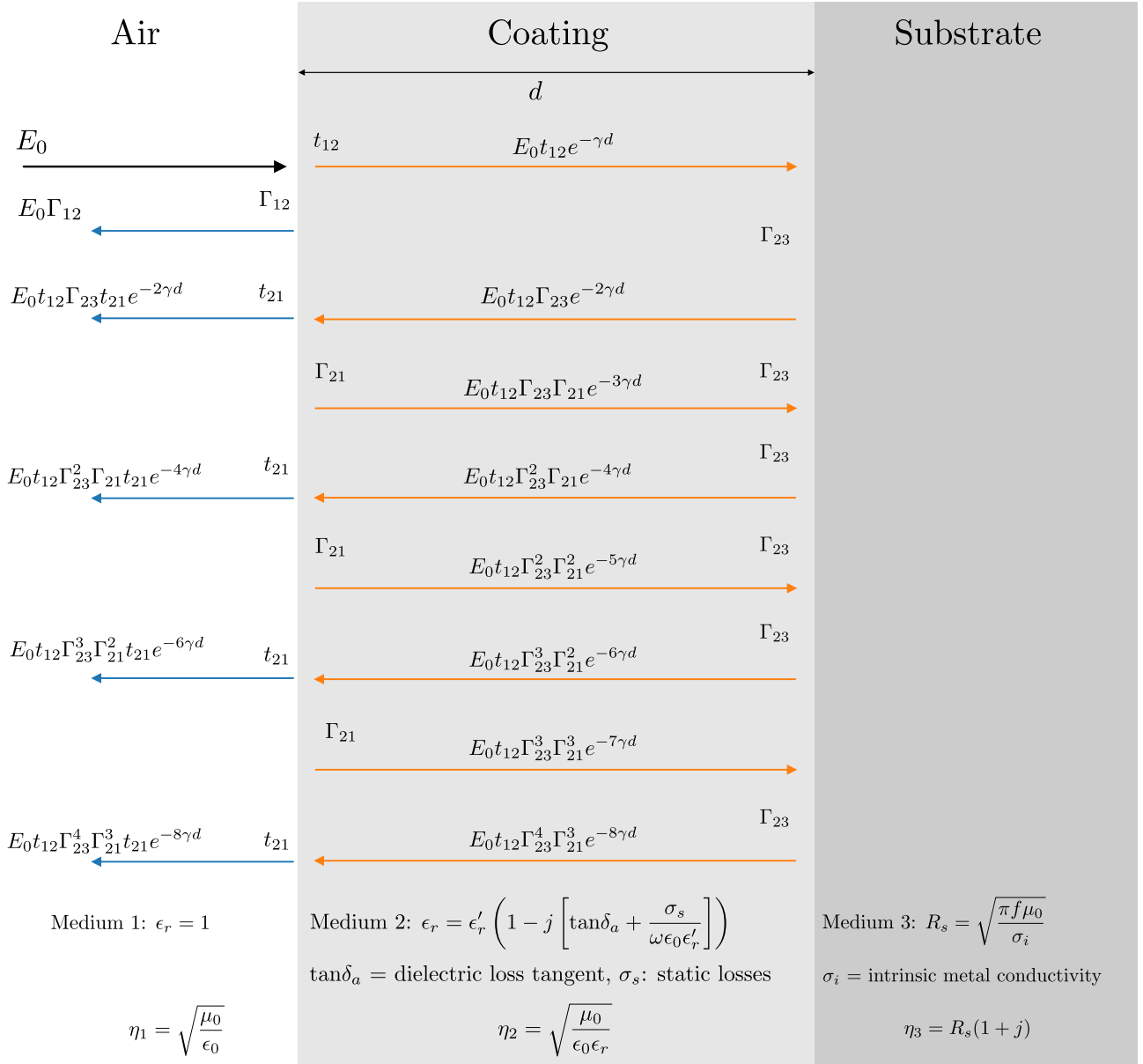can be used but at elevated temperatures the heating rate is no longer linear as radiation becomes important.

Figure 12. Heating rate of the ITER window sensors

References

1. R.C. Wolf et al., Performance of Wendelstein 7-X stellarator plasmas during the first divertor operation phase, Phys. Plasmas 26, 082504 (2019).
2. H.P. Laqua et al., The ECRH-Power Upgrade at the Wendelstein 7-X Stellarator, this conference.
3. H.P. Laqua et al., *ECRH Heating Scenarios and In-Vessel Components at the Wendelstein7-X Stellarator*, 28th EPS Onference on Contr. Fusion and Plasma Phys. Funchal, 18-22 June 2001. ECA Vol. 25A (2001) 1277-1280.
4. M. Hirsch et al., *The Impact of Microwave Stray Radiation to In-Vessel Diagnostic Components*, in: International Conf. on Fusion Reactor Diagnostics, Varenna, 9 - 13 September, 2013, AIP Conference Proceedings 1612, 39 (2014)
5. D. Hathiramani et al., *Microwave stray radiation: Measures for steady state diagnostics at Wendelstein 7-X*, Fusion Engineering and Design 88 (2013) 12321235
6. H.J. Hartfuss et al., *Problems with ECRH stray radiation in Wendelstein 7-X*, 30th EPS Conference on Contr. Fusion and Plasma Phys., St. Petersburg, 7-11 July 2003 ECA Vol. 27A, O-3.2C
7. J.W. Oosterbeek et al., *Microwave stray radiation losses in vacuum windows*, accepted for publication, Fusion Engineering and Design, 2022
8. H.P. Laqua et al., *Distribution of the ECRH stray radiation in fusion devices*, Proceedings of the 14th Joint Workshop on Electron Cyclotron Emission and Electron Cyclotron Resonance Heating, Santorini, Greece, 9-12 May 2006
9. D. Moseev et al., *Stray radiation energy fluxes in ITER based on a multiresonator model*. Fusion Engineering and Design 172 (2021)
10. Miriam Floristán, et al., *Development and testing of 140 GHz absorber coatings for the water baffle of W7-X cryopumps*, Fusion Engineering and Design 86 (2011) 1847-1850.
11. Andreas Killinger et al., *Plasma Spraying of a Microwave Absorber Coating for an RF Dummy Load*, MPDI Journal, Coatings 2021, 11, 801
12. Andreas Hentrich et al., *Resonant Atmospheric Plasma-Sprayed Ceramic Layers Effectively absorb Microwaves at 170 GHz*, Journal of Infrared, Millimeter, and Terahertz Waves (2022)
13. C.A. Balanis. *Advanced Engineering Electromagnetics*. John Wiley and Sons, 1986
14. Private Communication, Andreas Hentrich, Burkhard Plaum, EC21, 20-24 June 2022, ITER
15. F. Königer, *Measurement system for the precise determination of dielectrical properties in the mm-wave range based on hemispherical open resonators*, Frequenz 43 (1989)
16. I. Danilov, R. Heidinger, *New approach for open resonator analysis for dielectric measurements at mm-wavelengths*, Journal of the European Ceramic Society 23 (2003), 2623-2626
17. Samual. Y. Liao, *Microwave devices and circuits*, Prentice Hall, 1990, Third Edition
18. Private communication, Rafael Zubieta, Philippe Maquet, Sunil Pak

Appendix A: Model of coating response to incident plane wave

Air	Coating	Substrate

$\longleftrightarrow d$

E_0

t_{12} $E_0 t_{12} e^{-\gamma d}$

$E_0 \Gamma_{12}$ Γ_{12}

Γ_{23}

$E_0 t_{12} \Gamma_{23} t_{21} e^{-2\gamma d}$ t_{21} $E_0 t_{12} \Gamma_{23} e^{-2\gamma d}$

Γ_{21} $E_0 t_{12} \Gamma_{23} \Gamma_{21} e^{-3\gamma d}$ Γ_{23}

Γ_{23}

$E_0 t_{12} \Gamma_{23}^2 \Gamma_{21} t_{21} e^{-4\gamma d}$ t_{21} $E_0 t_{12} \Gamma_{23}^2 \Gamma_{21} e^{-4\gamma d}$

Γ_{21} $E_0 t_{12} \Gamma_{23}^2 \Gamma_{21}^2 e^{-5\gamma d}$ Γ_{23}

Γ_{23}

$E_0 t_{12} \Gamma_{23}^3 \Gamma_{21}^2 t_{21} e^{-6\gamma d}$ t_{21} $E_0 t_{12} \Gamma_{23}^3 \Gamma_{21}^2 e^{-6\gamma d}$

Γ_{21} $E_0 t_{12} \Gamma_{23}^3 \Gamma_{21}^3 e^{-7\gamma d}$

Γ_{23}

$E_0 t_{12} \Gamma_{23}^4 \Gamma_{21}^3 t_{21} e^{-8\gamma d}$ t_{21} $E_0 t_{12} \Gamma_{23}^4 \Gamma_{21}^3 e^{-8\gamma d}$

Medium 1: $\epsilon_r = 1$

Medium 2: $\epsilon_r = \epsilon_r' \left(1 - j \left[\tan\delta_a + \dfrac{\sigma_s}{\omega\epsilon_0\epsilon_r'} \right] \right)$

$\tan\delta_a$ = dielectric loss tangent, σ_s: static losses

Medium 3: $R_s = \sqrt{\dfrac{\pi f \mu_0}{\sigma_i}}$

σ_i = intrinsic metal conductivity

$\eta_1 = \sqrt{\dfrac{\mu_0}{\epsilon_0}}$

$\eta_2 = \sqrt{\dfrac{\mu_0}{\epsilon_0\epsilon_r}}$

$\eta_3 = R_s(1 + j)$

γ = propagation constant = $j\omega\sqrt{\mu_0\epsilon_0\epsilon_r'}\sqrt{1 - j\left(\tan\delta_a + \dfrac{\sigma_s}{\omega\epsilon_0\epsilon_r'}\right)} = \alpha + j\beta$.   MISTRAL work: $\left[\tan\delta_a + \dfrac{\sigma_s}{\omega\epsilon_0\epsilon_r'}\right] = \tan\delta$

$\Gamma_{12} = \dfrac{\eta_2 - \eta_1}{\eta_1 + \eta_2}$ $\Gamma_{23} = \dfrac{\eta_3 - \eta_2}{\eta_2 + \eta_3}$ $\Gamma_{21} = \dfrac{\eta_1 - \eta_2}{\eta_1 + \eta_2}$ $t_{12} = \dfrac{2\eta_2}{\eta_1 + \eta_2}$ $t_{21} = \dfrac{2\eta_1}{\eta_1 + \eta_2}$

$\Gamma_{sum} = \Gamma_{12} + t_{12}t_{21}\displaystyle\sum_{n=1}^{n=\infty} \Gamma_{21}^{(n-1)}\Gamma_{23}^{(n)} e^{-2n\gamma d}$

Fractional reflected power: $R = \Gamma_{sum}\Gamma_{sum}^*$ Fractional absorbed power: $A = 1 - R$

Drawing from:
Constantine A. Balanis, *Advanced Engineering Electromagnetics.* John Wiley and Sons, 1986
Paul F. Goldsmith, *Quasioptical Systems*, IEEE Press, 1998